

## **Validated Computational Modelling Techniques for Simulating Melt Pool Ejecta In Laser Powder Bed Fusion Processing**

D. Butcher<sup>1</sup>, S.Christie<sup>2</sup>, S.G.R. Brown<sup>1</sup>, N.P. Lavery<sup>1</sup>

1 - College of Engineering, Swansea University, Bay Campus, Crymlyn Burrows, Swansea, SA1 8EN, UK

2 - Renishaw plc, Additive Manufacturing Products Division, Brooms Road, Stone Business Park, Stone, Staffordshire, ST15 0SH, UK

### **Abstract**

Industry currently require faster build rates from laser powder bed fusion processes. As such, higher power lasers and multi-laser systems are being explored. Due to instabilities in the melting process, material is ejected from the melt pool in the form of spatter and vapour. Previous work has shown that these ‘ejecta’ can result in attenuation of the laser and redeposition of larger particles onto the powder bed; which can lead to poor mechanical properties.

ANSYS Fluent was used to create a CFD model which was validated against hot wire anemometry results from Renishaw’s RenAM 500Q. This was then coupled with a Discrete Phase Model (DPM) to track the ejection of spatter and vapour from the melt pool through the chamber. This has led to a better understanding of the removal of ‘ejecta’, leading to increased mechanical properties and lower rates of build failure.

### **Introduction**

Additive Manufacturing (AM) is a rapidly developing process which offers end users an enhanced design freedom to conventional subtractive processes. The ability to produce complex geometries including lattice structures or internal cavities has obvious weight saving applications making this an attractive process for multiple sectors such as: aerospace [1], automotive, medical [2] and tooling.

AM processes can generally be divided into 3 categories: wire fed, directed deposition or powder bed. Within powder bed techniques there are several different methods including: Electron Beam Melting (EBM), Binder Jetting and Laser Powder Bed Fusion (LPBF). In this work we will be looking at the LPBF process; specifically comparing the performance of the gas flow systems, and its subsequent effect on ejecta removal in the Renishaw AM250 and the RenAM 500Q using computational fluid dynamics.

In order to generate a part in the LPBF process first a ‘watertight’ CAD model must be constructed and transferred to the slicer via a stereolithography (stl) file. The component is then orientated on the virtual build plate; if supports are required, they are added at this stage. Following this, the geometry is ‘sliced’ into layers perpendicular to the plane of the build plate, in a desired layer thickness selected by the user. Finally, a build file is exported to the machine, which contains the laser scan paths for each layer and parameters to be used for each part on the build plate. In LPBF an inert atmosphere is required to prevent oxidation of the material during processing, before

a build can take place, the machine must be purged of oxygen. Secondly, the base plate is pre-heated to a set temperature depending on the machine. Once these requirements have been met the build can commence. The build plate is lowered by the desired layer thickness and powder is dosed across the bed. A laser is then used to selectively melt the powder defined by the build file, the now molten material then cools and solidifies. Once all the scan paths for a given layer have been completed, the build plate is lowered once again by the desired layer thickness, another layer of powder is dosed across the bed. This process repeats until the entire part specified has been built. Upon completion the unused powder material is separated from the part and sieved to recycle it to be feedstock material once again.

The by-products produced in LPBF are formed during the melting of the material; when the vaporization temperature of the material is reached a phase transformation takes place whereby metal vapour is produced forming a vapour plume. This vapour plume can attenuate the laser, therefore reducing the amount of energy being delivered to the bed. Furthermore, the pressures induced can result in the entrainment of particles into the melt pool [3] and create instabilities in the melt tracks [4]. Combined, these two factors can result in poor fusion of the powder which will result in reduced mechanical properties in the part being produced [5].

The recoil pressure and the subsequent flows induced, caused by the evaporation, can also eject molten metal and particles from the metal pool and surrounding bed. These larger particles being ejected from the melt pool and bed are generally known as spatter. Spatter can cause problems when it redeposits back onto the powder bed, as the laser can scan over these larger particles. This essentially results in a localised thicker layer, which in turn can result in incomplete fusion of material. Furthermore, any molten metal ejected will have a higher affinity to oxygen, which if processed by the laser will lead to greater oxygen content in the built part [5]. Oxygen is known to embrittle components and reduce fatigue life.

The inert gas system is utilised to remove the ejecta produced during melting, ideally from the entire chamber, but most importantly to prevent re-deposition back onto the powder bed or disturbance of the laser and the melting process. The uniformity and localised velocity have been shown previously to affect the final part quality [6].

This work presented aims to gain better understanding of the flow characteristics and its subsequent effect on the transport of melt pool ejecta through the use of simulation. It is hoped that further understanding will be gained by comparing the latest Renishaw platform the RenAM 500Q with previous work modelling the Renishaw Ren AM250.

### **Test Methodology**

In order to validate the original model a hot wire anemometer (HWA), Airflow TA 465 Series, was used to characterise the velocity profile on two planes above the base plate in the Renishaw AM250; one 3 mm above the plate and one in the centre plane of the inlet (37.5 mm). The velocity was recorded and averaged over a 20 second period at 66 points; spaced 50 mm apart width wise and at 25 mm depth intervals. In order to represent the processing conditions accurately, a perspex screen was produced with a series of holes to allow the HWA to be passed into the chamber. The unused holes were plugged to prevent leakage and represent the door.

As previously stated, the chamber is purged prior to a build commencing; Renishaw systems utilise a vacuum cycle prior to back filling with argon, to minimise the use of argon to create an inert atmosphere below 1000 ppm of Oxygen. During these experiments air was used instead of argon as the perspex screen would not have withstood the vacuum cycle. This in conjunction with potential for any leakage introduced by screen was deemed a health and safety risk. It was determined that this would have a minimal effect on the fluid flow in the chamber due to similar properties. Air and argon have densities of  $1.225 \text{ kgm}^{-3}$  and  $1.622 \text{ kgm}^{-3}$  and viscosities of  $1.789 \times 10^{-5} \text{ kgms}^{-1}$  and  $2.215 \times 10^{-5} \text{ kgms}^{-1}$  respectively.

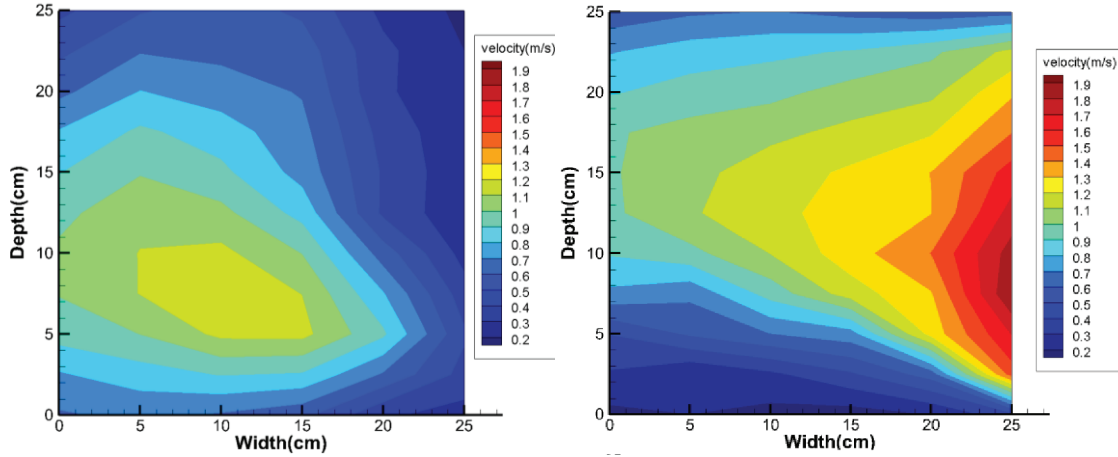


Figure 1 : Velocity contour maps of the Renishaw AM250 a) build plate plane (+3 mm) b) centre plane (+37.5 mm) [7]

The characterisation with the HWA has allowed the flow field to be visualised. As can be seen in Figure 1, the flow over the baseplate in the Renishaw AM250 is fairly inhomogeneous. It can be seen that there is a substantial region of lower velocity across the top of the build plate. This could be caused by the uneven flow in the centre plane, implying that the flow may not be leaving the inlet homogeneously.

### CFD Model

The equations governing the flow of viscous fluids are collectively known as the Navier-Stokes equations. They are based on the universal laws of mass and momentum conservation and the assumption that Reynolds stresses are proportional to the mean gradient of velocity. The equation for conservation of mass is

$$\frac{\delta(u_i)}{\delta x_i} = 0 \quad (1)$$

Conservation of momentum is expressed as follows

$$\rho u_j \frac{\delta u_i}{\delta x_j} + \frac{\delta p}{\delta x_i} - \frac{\delta \tau_{ij}}{\delta x_j} = 0 \quad (2)$$

Where  $\rho$  is the fluid density,  $u$  is the velocity and  $x$  is the spatial component. Where

$$\frac{\delta \tau_{ij}}{\delta x_j} = \mu \left( \frac{\delta u_i}{\delta x_j} + \frac{\delta u_j}{\delta x_i} \right) \quad (3)$$

Where  $\mu$  is the viscosity

Whilst the Navier-Stokes equations can be used to resolve flows across all turbulent length scales, the computing power required for this is unpractical. As such a time averaging approach is applied to the variables and can be described by:

$$\phi = \bar{\phi} + \phi' \quad (4)$$

Where,  $\phi$  is the mean value,  $\phi'$  is the fluctuating component and thus the time averaged component can be calculated from:

$$\bar{\phi} = \frac{1}{T} \int_{t_0}^{t_0+T} \phi(t) dt \quad (5)$$

By using the time averaged approach and assuming the time averaged fluctuations are equal to zero; the equations for conservation of mass and momentum can now be expressed as:

$$\frac{\delta \bar{u}_i}{\delta x_i} = 0 \quad (6)$$

$$\rho \bar{u}_j \frac{\delta (\bar{u}_i)}{\delta x_j} + \frac{\delta \bar{p}}{\delta x_i} + \frac{\delta (\overline{\rho u'_j u'_i})}{\delta x_j} - \frac{\delta \bar{\tau}_{ij}}{\delta x_j} = 0 \quad (7)$$

When using the Reynolds averaged Navier Stoke formulation for turbulence modelling the Reynolds stress term is an unknown value and must be modelled in order to solve the equations. Several turbulence models including: Spalart-Allmaras, k- $\epsilon$  and k- $\omega$  models; all use the Boussinesq hypothesis which relates the mean velocity gradients to the Reynolds stresses in the following manner:

$$\overline{\rho u'_j u'_i} = \mu_t \left( \frac{\delta u_i}{\delta x_j} + \frac{\delta u_j}{\delta x_i} \right) - \frac{2}{3} \left( \rho k + \mu_t \frac{\delta u_k}{\delta x_k} \right) \quad (8)$$

This approach is generally considered to be computationally inexpensive as only one or two transport equations need to be solved to compute the turbulent viscosity,  $\mu_t$ . In the case of the k- $\epsilon$  model two variables are solved for to calculate  $\mu_t$ : the turbulent kinetic energy,  $k$  and the turbulent dissipation rate,  $\epsilon$ . This approach assumes that the turbulent viscosity is an isotropic

scalar which is generally applicable to flows dominated by dominated by only one turbulent shear stresses. Further models have been developed such as the Reynolds stress model which solve a transport equation for all the terms in the Reynolds stress; this requires seven additional equations be solved to computer the turbulent viscosity. Generally, this additional computational expense is only beneficial in highly swirling flows.

The k- $\epsilon$  realizable model is modification of the traditional k- $\epsilon$  model, it utilises a new formulation to calculate turbulent viscosity from k and  $\epsilon$  and the transport equation for  $\epsilon$  has a modified formulation based upon the mean-square vorticity fluctuation. The respective transport equations for k and  $\epsilon$  are respectively

$$\frac{\delta(\rho k)}{\delta t} + \frac{\delta(\rho k u_i)}{\delta x_i} = \frac{\delta}{\delta x_j} \left[ \left( \mu + \frac{\mu_t}{\sigma_e} \right) \frac{\delta k}{\delta x_j} \right] + G_k + G_b - \rho \epsilon - Y_m + S_k \quad (9)$$

$$\frac{\partial \rho \epsilon}{\delta t} + \frac{\delta(\rho \epsilon u_i)}{\delta x_i} = \frac{\delta}{\delta x_j} \left[ \left( \mu + \frac{\mu_t}{\sigma_e} \right) \frac{\delta \epsilon}{\delta x_j} \right] + \rho C_1 S_\epsilon - \rho C_2 \frac{\epsilon^2}{k + \sqrt{v \epsilon}} + C_{1\epsilon} \frac{\epsilon}{k} C_{3\epsilon} G_b + S_\epsilon \quad (10)$$

Where,

$$C_1 = \max \left[ 0.43, \frac{v}{v + 5} \right] \quad (11)$$

$$v = S \frac{k}{\epsilon} \quad (12)$$

$$S = \sqrt{2 S_{ij} S_{ij}} \quad (13)$$

Traditionally in k- $\epsilon$  models the turbulent viscosity is calculated using the following equation.

$$\mu_t = \rho C_\mu \frac{k^2}{\epsilon} \quad (14)$$

Where  $C_\mu$  is an empirically derived value of 0.09 however in the realizable model this term is solved from

$$C_\mu = \frac{1}{A_0 + A_s \frac{k U^*}{\epsilon}} \quad (15)$$

Where,

$$U^* = \sqrt{S_{ij} S_{ij} + \widetilde{\Omega}_{ij} \widetilde{\Omega}_{ij}} \quad (16)$$

$$\widetilde{\Omega}_{ij} = \Omega_{ij} - 2\varepsilon_{ijk}\omega_k \quad (17)$$

$$\Omega_{ij} = \overline{\Omega}_{ij} - 2\varepsilon_{ijk}\omega_k \quad (18)$$

$\widetilde{\Omega}_{ij}$  is the mean rate of rotation tensor in a moving reference frame where  $\omega_k$  is the angular velocity. Finally,  $A_0 = 4.04$  and the model constants can be calculated from the following:

$$A_s = \sqrt{6} \cos \phi \quad (19)$$

$$\phi = \frac{1}{3} \cos^{-1}(\sqrt{6}W) \quad (20)$$

$$W = \frac{S_{ij}S_{jk}S_{ki}}{\bar{S}^3} \quad (21)$$

$$S_{ij} = \frac{1}{2} \left( \frac{\partial u_j}{\partial x_i} + \frac{\partial u_i}{\partial x_j} \right) \quad (22)$$

Turbulent flows are significantly affected by the presence of walls, the viscosity affected region known as the boundary layer has large gradients in solution variables. Consequently, an accurate representation of the boundary layer is required in order to successfully model wall bounded flows.

Generally, there are two methods to modelling the boundary layer, the first is near wall modelling. In this approach the turbulence models must be modified for low Reynolds conditions, to enable them to resolve the viscous boundary layer. This in turn necessitates that the mesh is refined right up to the wall, which results in a much larger mesh and subsequently much more computational resources are required.

The second approach is known as wall functions, these are a set of empirically derived equations used to predict the flow characteristics in the viscous region. This means that the turbulence models don't need to be adjusted for low Reynolds conditions and that the mesh does not require resolving right up to the wall subsequently, this reduces the computational expense of the simulation. Standard wall functions use the law of the wall to calculate the velocity between the wall and the fully turbulent region. The law of the wall is defined by:

$$U^* = \frac{1}{k} \ln(Ey^*) \quad (23)$$

Where  $U^*$  is the dimensionless velocity and  $y^*$  is the dimensionless distance from the wall and they are defined by the following equations:

$$U^* \equiv \frac{U_p C_\mu^{1/4} k_p^{1/2}}{\tau_w / \rho} \quad (24)$$

$$y^* = \frac{\rho C_\mu^{1/4} k_p^{1/2} y_p}{\mu} \quad (25)$$

Where  $k$ , is the Von Karman constant (0.4187),  $E$  is the empirical constant (9.793),  $U_p$  is the mean velocity of the fluid at the wall-adjacent cell centroid  $P$ ,  $k_p$  is the turbulent kinetic energy at the wall adjacent cell centroid  $P$ ,  $y_p$  is the distance from the centroid of the wall adjacent cell to the wall  $P$  and finally,  $\mu$  dynamic viscosity of the fluid [7].

Standard wall functions necessitate that the first cell centre must fall within the log-law region of the boundary layer and satisfy a specific  $y^*$  value range to ensure the boundary layer is resolved correctly and consequently the accuracy of the simulation.

There are several modified wall functions available within ANSYS Fluent, all of which have an improvement over standard wall functions. Menter Lechner wall functions have been developed to attempt to avoid the sensitivity of standard wall functions to the  $y^*$  value.

Due to the known computational benefits of hexahedral meshes a cartesian cut cell assembly meshing procedure as used to generate the mesh within the ANSYS workflow. This allowed a mesh to be constructed which was composed of 98.9 % hexahedral elements, with minimal amounts of tetrahedral, prismatic and wedge style elements. A total of 5.7 million elements were required to achieve an average orthogonal quality of 0.98 and an average aspect ratio of 1.05.

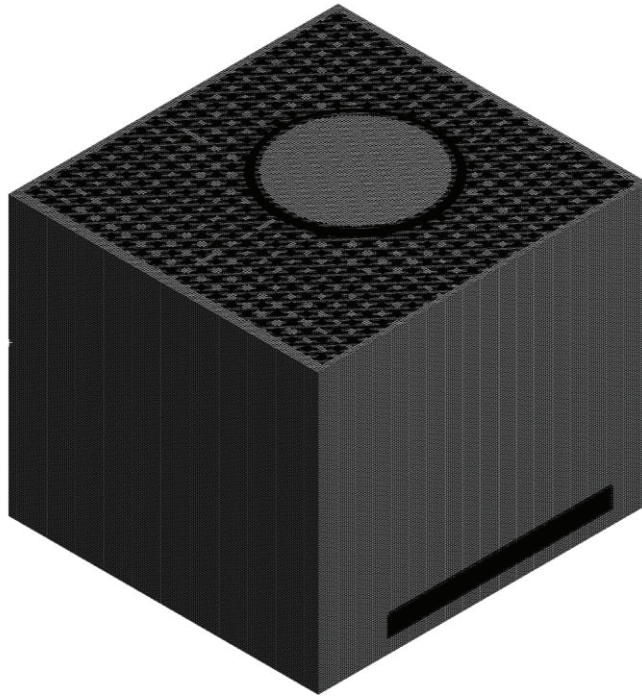


Figure 2 : Surface mesh of the RenAM 500Q used for the simulations



The Reynolds number was calculated using an estimated flow velocity through the inlet of 3.5 m/s and the hydraulic diameter of the square inlet of 0.021 m. This resulted in an estimated Reynolds number of 5,400 placing it in the turbulent regime.

A mass flow boundary condition was used to define all the inlets present in the model. The mass flow rate for the inlets was derived from the volumetric flow rate of the closed loop gas system which was set to 180 m<sup>3</sup>hr<sup>-1</sup> using equation 26, which resulted in a mass flow rate of 0.02705 kgs<sup>-1</sup>, for the lower inlets. An outflow boundary condition was used at the outlet to conserve mass in the model.

$$\dot{m} = \rho \dot{v} \quad (26)$$

The solver used for these simulations was ANSYS Fluent in a three-dimensional, steady, incompressible formulation. Pressure and momentum were coupled using the SIMPLE (Semi-Implicit Method for Pressure Linked Equations) algorithm.

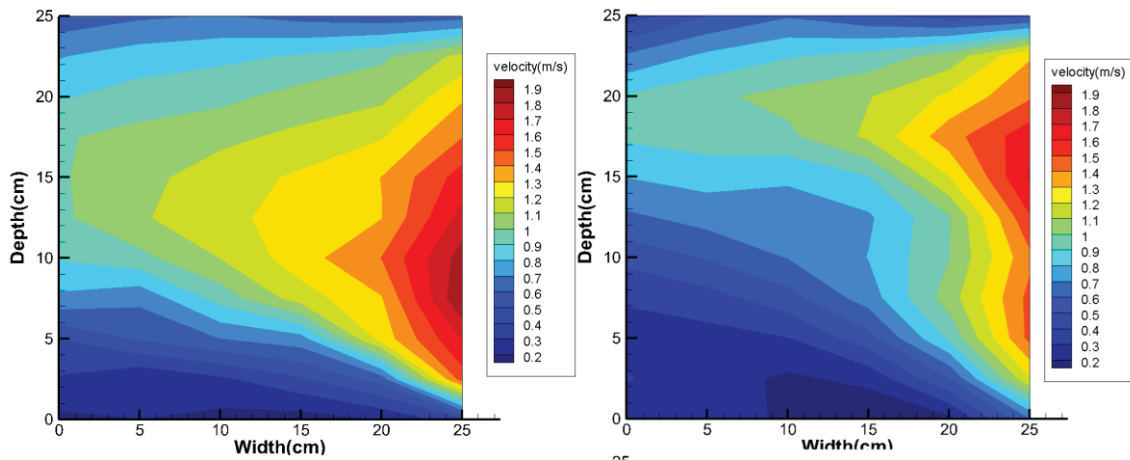


Figure 3: Velocity contour map comparing the base plate plane (+3 mm) a) the HWA results b) the CFD prediction

As can be seen in Figure 3 the simulation has captured most of the flow characteristics across the base plate plane. Whilst some differences are to be expected due to the defeaturing of the geometry; namely excluding the hopper and wiper from the model, despite this the overall trends are captured.

In order to evaluate the performance of each machine two performance indicators have been selected: the area weighted average velocity and the area weighted uniformity index were calculated for the plane 3 mm above the build plate. The area weighted average of a variable is calculated through:

$$\overline{\phi_a} = \frac{\sum_{i=1}^n \phi_a A_i}{\sum_{i=1}^n A_i} \quad (27)$$

This can then be used to calculate the uniformity through the following equation:



$$\gamma = 1 - \frac{\sum_{i=1}^n [(|\phi_i - \overline{\phi_a}| A_i)]}{2|\overline{\phi_a}| \sum_{i=1}^n A_i} \quad (28)$$

Where a value of 1 would represent a perfectly uniform flow.

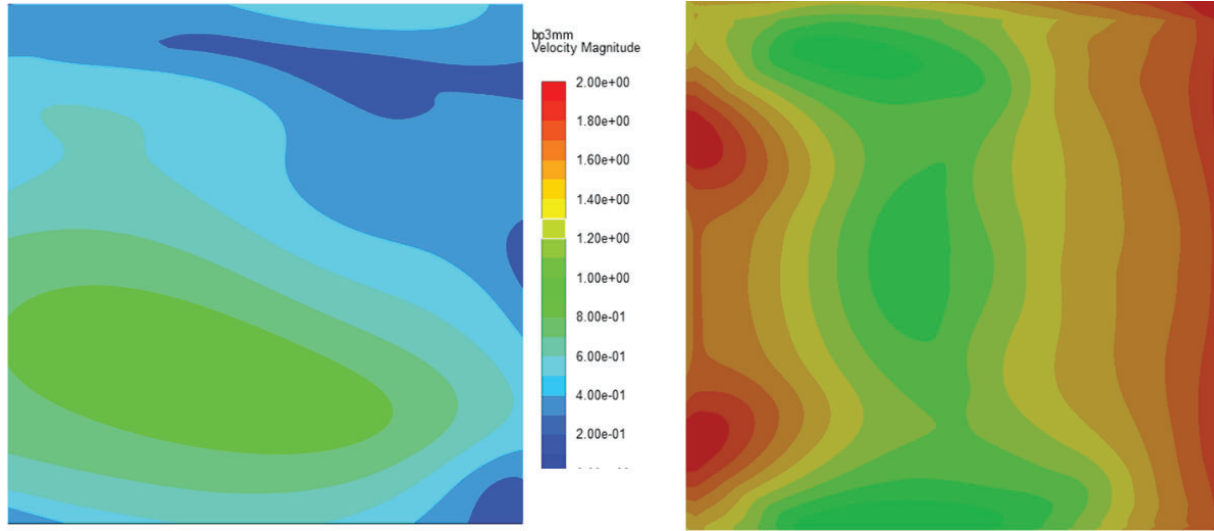


Figure 4: Velocity contour map as predicted by the CFD model a) Ren AM250 b) RenAM 500Q

It can be seen in Figure 4 that flow over the build plate in the RenAM 500Q has a clearly higher average velocity across the baseplate and is more homogenous than the AM250. Each have a respective area weighted average velocity of  $0.6 \text{ ms}^{-1}$  and  $1.6 \text{ ms}^{-1}$ , this represents a substantial increase in velocity of 167 %. Area weighted uniformity has also been substantially improved from 0.82 to 0.93 in the 500Q. This data is summarised in Table 1.

Machine	Average Velocity	Uniformity
Ren AM250	$0.6 \text{ ms}^{-1}$	0.82
RenAM 500Q	$1.6 \text{ ms}^{-1}$	0.93

Table 1: Average velocity and uniformity data as predicted by the CFD model

Furthermore, it can be seen in Figure 5 that the model predicts that there are two recirculation flows in the Ren AM250; one coming back against the flow along the front of the machine, and the second going up the back left corner. In comparison, the RenAM 500Q does not exhibit the same trends and has a much more stable flow pattern which is expected to have contributed to the improved uniformity.

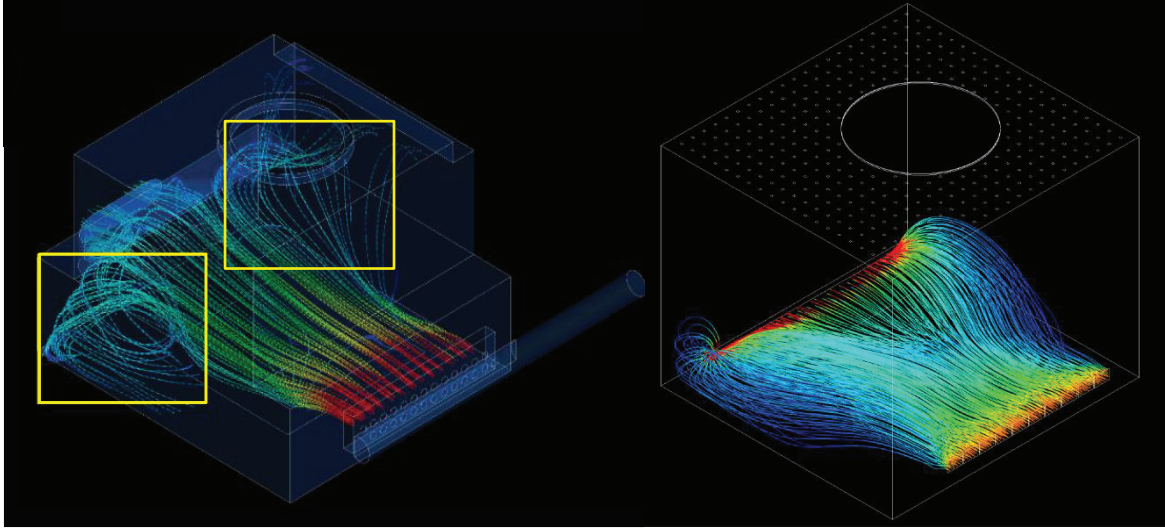


Figure 5: Streamlines showing predicted flow characteristics of the a) AM250, b) RenAM500Q

### **Representative Spatter Expulsion Model**

A Discrete Phase Model (DPM) was selected to model the transport of the spatter particles within the chamber. This meant that modelling the complex fluid flows at the melt pool scale could be avoided, as the inputs for the DPM could be provided by experimental analysis. The DPM allows for a secondary phase to be introduced and is tracked in a Lagrangian frame of reference through the flow field. In order to incorporate the data from experimental analysis of the spatter to the DPM a User Defined Function (UDF) was written. The UDF determines the random release of particles into the chamber, based on the statistical distribution from the experimental data. Two-way coupling was enabled between the discrete and continuous phase in order to calculate particle accumulation on surfaces. Three assumptions are made in the set-up of the DPM:

1. Particle – particle interactions are neglected, as they were not observed in the experiment
2. Particles are spherical, so spherical drag law can be used
3. No bias based on weld mode or direction

The DPM calculates the trajectory of a discrete particle by integrating the force balance acting on the particle. This force balance equates the particle inertia with the forces acting on the particle, which can be expressed as:

$$\frac{d\vec{u}_p}{dt} = \frac{\vec{u} - \vec{u}_p}{\tau_r} + \frac{\vec{g}(\rho_p - \rho)}{\rho_p} + \vec{F} \quad (29)$$

Where  $\vec{u}$  is the fluid phase velocity,  $\vec{u}_p$ ,  $\vec{\rho}$  is the fluid phase density,  $\vec{\rho}_p$  is the particle density and  $\vec{g}$  is the gravitational force. The  $\vec{F}$  term accounts for additional acceleration forces.  $\tau_r$  is the particle relaxation time which is defined as:

$$\tau_r = \frac{\rho_p d_p^2}{18\mu} \frac{24}{C_d Re} \quad (30)$$

Where  $d_p$  is the particle diameter,  $\mu$  is the molecular viscosity of the fluid and  $Re$  is the relative Reynolds number defined as:

$$Re = \frac{\rho d_p |\vec{u}_p - \vec{u}|}{\mu} \quad (31)$$

And  $C_d$  is the coefficient of drag using the spherical drag law is defined as:

$$C_d = a_1 + \frac{a_2}{Re} + \frac{a_3}{Re^2} \quad (32)$$

Where  $a_1$ ,  $a_2$  and  $a_3$  are constants that apply over several range of  $Re$  given by Morsi and Alexander [8]. Finally, the trajectory of a particle is predicted by:

$$\frac{dx}{dt} = u_p \quad (33)$$

Equations 29 and 33 are solved for each particle trajectory via a stepwise integration over discrete time steps. Integration of these equations gives the velocity of each particle at each time step along the trajectory [7].

In order to determine the velocity magnitudes and vectors of the spatter particles being ejected from the melt pool, a high-speed imaging camera (FASTCAM SA4 500K-M1) was used to record the ejection of particles during a build of 316L Stainless Steel. Operating at 3600 frames per second with a resolution of 1024 x 640, the camera was found to be adequate to capture the geometry of the spatter whilst allowing a high enough frame rate for analysis.

The Mosaic suite for ImageJ was used to analyse the images recorded from the high-speed camera. First of all, the images were 'cleaned up' to sharpen the image and allow particles to be identified more readily. Following this the particles could be identified and labelled. Particles are identified based on their radius, which is derived from the number of pixels across the diameter of the particle. The script then tracks each particle through each of the high-speed image frames recorded, reporting the location of each particle in each frame as pixel location in the image. Finally, this data was passed to Matlab where it was analysed using an in-house script to determine the velocity and vector of each particle. The spatter particles velocity was found to be between 0-8 ms<sup>-1</sup> and, there appeared to be no bias based on weld direction. These results are comparable with other work found in the literature. Zhao et al. [9] used a high-speed Synchrotron to calculate the velocities of Ti-6Al-4V spatter particles and found that the velocities fell between 0-12 ms<sup>-1</sup>. This is comparable with the data collected; it is expected that the differences are the result of the varying material densities or the difference in laser parameters. Secondly, Bidare et al. [10] used a finite element model to predict the argon flow induced from the evaporation of material in the melt pool; their model predicts speeds of up to 10 ms<sup>-1</sup> which gives us more confidence in our results.

Generally, before powder is recycled in the LPBF process it is sieved either manually or automatically before being reintroduced to the feedstock material. The size fraction removed by the sieve was analysed using a Malvern Mastersizer which showed the sizes of spatter particles ranged from 60-120  $\mu\text{m}$ .

Liu et al. [5] used Energy-dispersive X-ray Spectroscopy (EDS) to determine that spatter particulates composition was greater in oxygen than that of the feedstock material. It was consequently considered to be negligible with respect to the thermal and physical properties, consequently standard material properties were used for Stainless Steel 316L for the spatter particles in the DPM.

This approach was previously validated for the Ren AM 250 [11]. As can be seen in Figure 6 the model predicts that minimal spatter will accumulate at the front chamber; whilst predicting the majority would land under the outlet and towards the back of the machine. Subsequently, samples of powder were collected from the front of the machine and under the outlet after a large part build. The powder size distribution of the sample gathered from the front of the machine was within 2 % of the feedstock material sampled before the build. In contrast the sample gathered from under the out contained a large number of large particles deemed to be spatter particles.

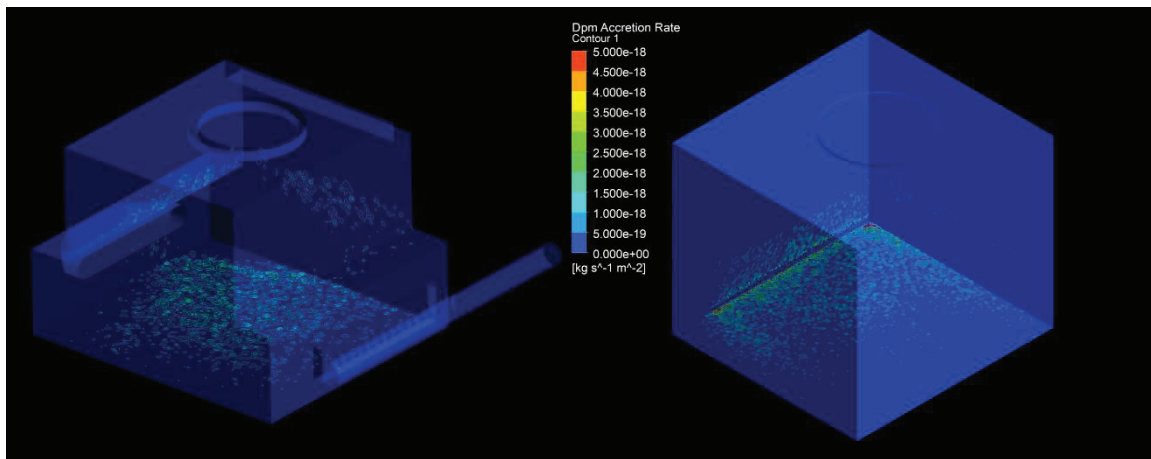


Figure 6: Visualisation of spatter accumulation in the chamber as predicted by the DPM: a) Ren AM250 b) RenAM 500Q

It can be seen in Figure 6 that the predicted improved flow properties of the RenAM 500Q have had a substantial effect on the transport of the spatter within the chamber. The model predicts that in the Ren AM250 spatter will accumulate under the outlet, at the back of the chamber and up the side of the walls. In contrast it is predicted that in the RenAM 500Q the spatter will mainly be focused around the outlet.

Table 2 summarises the predicted spatter accumulation locations for both machines. The model predicts that a third of the spatter will be removed in the RenAM 500Q which is huge improvement over the Ren AM250. More importantly, it is predicted that in the 500Q less than half of particles will redeposit back on the base plate; 12 % as opposed to 29 % respectively.

Machine	% Spatter Build Plate	% Spatter Walls	% Spatter Escaped
Ren AM250	29 %	71 %	0 %
RenAM 500Q	12 %	55%	33 %

Table 2: Spatter accumulation as predicted by the model for Ren AM250 and RenAM500Q

### **Conclusions and Future Work**

In this work a computational fluid dynamic, which has been shown to be within 10-20 % of experimental results on the Ren AM250, has been applied to the latest Renishaw LPBF machine the RenAM 500Q. The modelling of the 500Q has predicted two things about the flow characteristics in the new chamber; firstly, that the average velocity over the processing area will be improved to  $1.6 \text{ ms}^{-1}$  an almost 167% improvement compared to the Ren AM250. Secondly, that the uniformity would be substantially improved from 0.82 on the Ren AM250 to 0.92 with substantially less recirculation seen in the RenAM 500Q.

A representative spatter expulsion model was coupled to the CFD model, using a Eulerian-Lagrange formulation in order to predict the spatter transport inside the chamber. Experimental evidence suggests that the spatter accumulates in the same areas as predicted by the model. The model predicts that 17 % less spatter will land back on the processing area; which according to the literature should lead to improved mechanical properties parts produced. When observing a build on the 500Q a noticeable improvement can be visually observed in the removal of spatter however unfortunately it at this time it has not been possible to validate the model for the 500Q.

Future work will aim to model the vapour phase using the same discrete phase model as the representative spatter expulsion model, with an additional white noise source introduced to model the Brownian motion exhibited by small particles. It is hoped these models can be used a design tool to control the transport of ejecta in the LPBF process.

### **Acknowledgements**

The authors would like to acknowledge and thank the Additive Manufacturing Products Division at Renishaw Plc. and the M2A funding from the European Social Fund via the Welsh Government (c80816) that has made this research possible. In addition, the authors would like to acknowledge the Materials Advanced Characterisation Centre (MACH1) for the use of state-of-the-art equipment funded by the Welsh Government and the Advanced Sustainable Manufacturing Technologies (ASTUTE 2020) funded by the Welsh European Funding Office.

### **Bibliography**

- [1] R. Liu, Z. Wang, T. Sparks, F. Liou and J. Newkirk, "Aerospace applications of laser additive manufacturing," in *Laser additive manufacturing*, Woodhead Publishing, 2017, pp. 351-371.

- [2] M. Munsch, "Laser additive manufacturing of customized prosthetics and implants for biomedical applications," in *Laser Additive Manufacturing*, Woodhead Publishing, 2017, pp. 399-420.
- [3] M. J. Matthews, G. Guss, S. A. Khairallah, A. M. Rubenchik, P. J. Depond and W. E. King, "Denudation of metal powder layers in laser powder bed fusion processes," *Acta Materialia*, vol. 114, pp. 33-42, 2016.
- [4] C. Qiu, C. Panwisawas, M. Ward, H. C. Basoalto, J. W. Brooks and M. M. Attallah, "On the role of melt flow into the surface structure and porosity development during selective laser melting," *Acta Materialia*, vol. 96, pp. 72-79, 2015.
- [5] Y. Liu, Y. Yang, S. Mai, D. Wang and C. Song, "Investigation into spatter behavior during selective laser melting of AISI," *Materials & Design*, vol. 87, pp. 797-806, 2015.
- [6] A. Ladewig, G. Schlick, M. Fisser, V. Schulze and U. Glatzel, "Influence of the shielding gas flow on the removal of process by-products in the selective laser melting process," *Additive Manufacturing*, vol. 10, pp. 1-9, 2016.
- [7] ANSYS, ANSYS Fluent Theory Guide, 2017.
- [8] S. A. Morsi and A. J. Akexander, "An Investigation of Particle Trajectories in Two-Phase Flow Systems," *Journal of Fluid Mechanics*, pp. 193-208, 1972.
- [9] C. Zhao, K. Fezzaa, R. W. Cunningham, H. Wen, F. D. Carlo, L. Chen, A. D. Rollett and T. Sun, "Real-time monitoring of laser powder bed fusion process using highspeed," *Scientific Reports*, vol. 7, 2017.
- [10] P. Bidare, I. Bitharas, R. Ward, M. M. Attallah and A. Moore, "Fluid and particle dynamics in laser powder bed fusion," *Acta Materialia*, vol. 142, pp. 107-120, 2018.
- [11] A. M. Philo, D. Butcher, C. J. Sutcliffe, J. Sienz, S. Brown and N. P. Lavery, "A Multiphase CFD Model for the Prediction of Particulate Accumulation in a Laser Powder Bed Fusion Process," in *TMS 2018*, 2018.